First-Principles-aided evaluation of the Nernst Coefficient beyond the Constant Relaxation Time approximation

S. Emad Rezaei¹, Mona Zebarjadi^{1,2}, and Keivan Esfarjani^{3,4}

¹University of Virginia, Department of Electrical and Computer Engineering

²University of Virginia, Department of Materials Science and Engineering ³University of Virginia, Department of Mechanical and Aerospace Engineering

⁴University of Virginia, Department of physics

Abstract

The solution of the Boltzmann Transport Equation (BTE) under open voltage conditions and in the presence of simultaneously applied magnetic field and temperature gradient results in the so-called Nernst response of the electrons. The calculation of the Nernst coefficient using first-principles calculations as an extension of the BoltzWann code and under Jones-Zener expansion valid for weak magnetic fields has been the subject of our previous work which provided a general framework for the calculation of the Nernst effect but was not able to capture the experimental results due to the constant relaxation time approximation used. In Contrast to the Seebeck coefficient which is not sensitive to the details of the relaxation times, the Nernst coefficient is proportional to the carrier mobility and hence is greatly affected by the relaxation times. In this work, we focus on the inclusion of the energy-dependent electron-phonon and the electron-impurity relaxation times in our formalism. Using the developed formalism, we successfully reproduced the experimental data of several samples. In this paper, we report our results on Ge, Si, and InSb samples. However, the code is not limited to the reported samples and supports a wide range of materials.

Keywords: Relaxation time, Nernst coefficient, Band velocity

1 Introduction

Energy harvesting plays a crucial role in the progress of the Internet of Things (IOT) to manage energy conversion and storage [1]. Thermoelectric (TE) devices that convert the waste heat into electrical energy perform on the principle of the Seebeck effect. A temperature gradient in a material causes the migration of the charge carriers, as a result, a voltage develops along

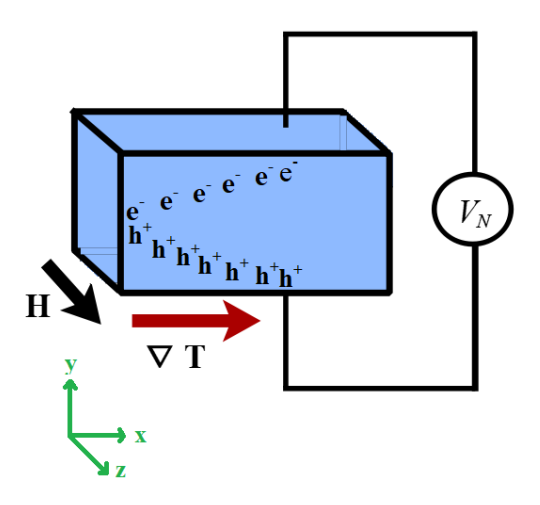


Figure 1: Schematic illustration of the Nernst effect. Electrons and holes move in opposite directions in the presence of an external magnetic field (H).

the temperature gradient. The ratio of the developed voltage difference to the temperature difference is the Seebeck coefficient which is a longitudinal signal. TE modules have been vastly utilized in many areas ranging from wireless sensor networks [2] to space crafts [3]. The Nernst effect is analogous to the Seebeck effect under an applied magnetic field. It is the basis of the thermomagnetic phenomenon. The advances in superconducting magnets facilitated the induction of strong magnetic fields. As a consequence, the Nernst effect was proposed for extended applications such as cryogenic cooling [4], thermal radiator detection [5], and thermopile systems [6].

Nernst and Ettingshausen [7] observed a cross-plane voltage in Bismuth under an external magnetic field and a temperature difference perpendicular to each other. The generated voltage is called the Nernst coefficient and was found to be particularly large for Bismuth at low temperatures [8]. The force acting on a moving charge in the presence of a magnetic field is expressed by the Lorentz force which causes their trajectory to curve: $(\vec{F} = q\vec{\nu} \times \vec{H})$ where H is the magnetic field, including the magnetic permittivity μ_0 , and is measured in Teslas.) Because of their opposite charge electrons and holes are pushed in opposite directions under a perpendicular magnetic field (see Fig. 1). The accumulation of electrons and holes on opposite sides of the sample generates the so-called Nernst voltage.

Studies on the Nernst effect started from metals and semimetals and continued by examining semiconductors, namely, Germanium [9, 10] and InSb [11]. Germanium was the first semiconductor that showed a remarkable Nernst signal at room temperature. As of today, germanium still holds the record for the largest Nernst coefficient at room temperature. Indium antimonide also emerged as a potential candidate for the Nernst-based applications at room temperature owing to its noticeable Nernst coefficient, nearly $100~\mu V/KT$, where the Nernst coefficient is defined as the ratio of transverse Nernst voltage gradient to the longitudinal temperature gradient and is reported per unit magnetic field.

Along with the measurements, efforts were made to model the Nernst coefficient. The earliest model was proposed by Moreau that describes the Nernst coefficient as a product of the electrical conductivity (σ) , Hall coefficient (R_H) , and Thompson coefficient $\tau = TdS/dT$ as $N = \sigma \tau R_H$. Moreau's equation was derived by making multiple thermodynamics and physical assumptions but was successful in explaining the Nernst coefficient measured in several metals. For the first time, Delves [12] analytically solved the Boltzmann transport equation (BTE) in

the presence of a magnetic field for spherical bands within relaxation time approximation. With the help of the Onsager relations and heat/electric current coupled equations, he derived the Nernst, Ettingshausen, and Hall coefficients and replicated the experimental results of HgSe. Later, the Nernst coefficient was estimated using the Mott's formula [13] for $Ni_{80}Fe_{20}$ and Ni thin films and produced the trend of the experimental data [14]. Apart from the fact that the Mott formula applies only to metals, it was found to fall far from the experimental Nernst coefficient values of $BaFe_2As_2$ and $CaFe_2As_2$ [15]. More recently, Heremans et.al. [16] applied a semi-empirical method to support their Nernst measurement. They performed a tight-binding model of a Weyl semimetal by taking a trigonometric Hamiltonian and obtained results relatively close to the experiments in the case of NbP.

The aforementioned models were empirical or semi-empirical, and although can explain the trends, cannot accurately predict the experimental results without fitting parameters. Besides, the effect of the electronic structure-dependent quantities such as group velocity and effective mass are oversimplified in such approaches. In our previous study [17] we presented an approach to calculate the Nernst coefficient using first-principles density functional theory within the constant relaxation time approximation. Unlike the Seebeck coefficient, the Nernst coefficient is proportional to the carrier mobility and hence is extremely sensitive to the details of the relaxation time. The constant relaxation time approximation is therefore insufficient to accurately predict the Nernst coefficient. Herein, we demonstrate a new approach to computing the Nernst coefficient including electron-phonon and ionized impurity scattering rates with the basis set of maximally-localized Wannier functions. Our method combines the scattering rates with the Boltzmann transport equation in the presence of a magnetic field and calculates the Nernst coefficient. The Nernst coefficients of germanium, silicon, and InSb are attained at a reasonable computational cost and our theoretical results are in fairly close agreement with the experiments.

2 Theoretical formalism

In our previous work [18], similar to the original work of Delves[12], we showed that the isothermal Nernst coefficient (N_T) in the presence of a magnetic field along the z-axis is the ratio of the developed voltage along the y-axis to the temperature difference along the x-axis and will be identified as $N_T = \alpha_{yx}(H)$ where:

$$\left[\alpha(H)\right] = \left[\sigma(H)\right]^{-1} \left[B(H)\right] \tag{1}$$

and the matrices σ and B are expressed in terms of the so-called transport distribution function $\Xi(\varepsilon)$ calculated from the solution of BTE:

$$\sigma_{ij}(H) = q^2 \int \Xi_{ij}^H(\varepsilon) \left(-\frac{\partial f(\varepsilon, \mu, T)}{\partial \varepsilon} \right) d\varepsilon$$
 (2)

$$B_{ij}(H) = \frac{q}{T} \int \Xi_{ij}^{H}(\varepsilon) \left(-\frac{\partial f(\varepsilon, \mu, T)}{\partial \varepsilon} \right) (\varepsilon - \mu) d\varepsilon$$
 (3)

where the indices i, j represent Cartesian indices, q the particle charge, T the temperature, μ the chemical potential, and finally f is the Fermi-Dirac distribution function. Within the relaxation time approximation, and in the limit of small magnetic fields $(\tau qH/m \ll 1)$, the transport distribution function is written, to linear order in H, as:

$$\Xi_{ij}^{H}(\varepsilon) = \frac{1}{VN} \sum_{n,k} \nu_{i,nk} \tau_{nk} [\nu_{j,nk} - \Omega \tau_{nk} \nu_{j,nk}] \delta(\varepsilon - \varepsilon_k)$$
(4)

where the pair nk refers respectively to the electron band and wave vector in the Brillouin zone, ν is the electron velocity vector, τ is the relaxation time, assumed to be only energy-dependent, V and N are the unit cell volume and number of k-points, respectively, and the "frequency operator" Ω is defined red in reciprocal space to be $\Omega = \frac{q}{\hbar}\nu \times H \cdot \nabla_k$. Its action on the product $\tau \nu_i$ is:

$$\Omega \tau \nu_j = q\tau(\varepsilon) \,\epsilon_{pqr} \,\nu_p \,H_q \,\left(\frac{1}{m}\right)_{rj} \tag{5}$$

where ϵ_{pqr} is the antisymmetric Levi-Civita symbol, $\frac{1}{\hbar} \left(\frac{\partial \nu_j}{\partial k_r} \right) = \left(\frac{1}{m} \right)_{jr}$ is the symmetric inverse effective mass tensor, and an implicit summation is assumed over repeated indices. In this equation, the electron energy, velocity, and effective mass are obtained from a band structure calculation (output of the Boltzwann code[19]), and the total relaxation time τ resulting from all scatterings is an output of the code AMSET. [20]

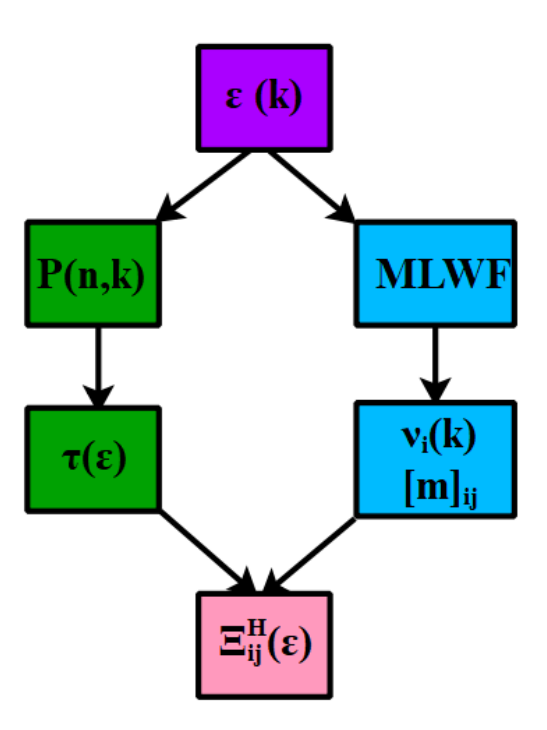


Figure 2: The workflow used in this work to calculate the Nernst coefficient. Wannier functions, group velocity, and effective mass tensor (blue boxes) come from the Wannier90 package[21]. Scattering rates (P) and relaxation times are taken from AMSET or similar codes (green boxes). We couple the output of the two codes to obtain the total transport distribution function (Ξ) .

Using the mentioned assumptions, the final expression for the transport distribution function becomes:

$$\Xi_{ij}^{H}(\varepsilon) = \frac{1}{VN} \sum_{n,k} \nu_{i,nk} \tau_{nk} \left[\nu_{j,nk} - q\tau(\varepsilon) \, \epsilon_{ulp} \, \nu_{u} \, H_{l} \left(\frac{1}{m} \right)_{pj} \right] \, \delta(\varepsilon - \varepsilon_{k}) \tag{6}$$

This distribution function is the sum of two terms: the first one is the standard one at zero magnetic field, and the second, linear in the magnetic field, assumed to be smaller than the

first, contains the magnetotransport response. Due to the parity symmetry of velocities, one can see that the off-diagonal elements of the matrices σ and B are linear in H. In contrast, the diagonal elements do not depend on H up to O(H).

Finally, the Seebeck and the isothermal Nernst coefficients up to terms linear in H can be written as

$$S = \alpha_{xx} = \frac{\sigma_{yy}B_{xx} - \sigma_{xy}B_{yx}}{\sigma_{xx}\sigma_{yy} + \sigma_{xy}^2} \simeq \frac{B_{xx}}{\sigma_{xx}} + O(H^2)$$
 (7)

$$S = \alpha_{xx} = \frac{\sigma_{yy}B_{xx} - \sigma_{xy}B_{yx}}{\sigma_{xx}\sigma_{yy} + \sigma_{xy}^{2}} \simeq \frac{B_{xx}}{\sigma_{xx}} + O(H^{2})$$

$$N_{T}(H) = \alpha_{yx} = \frac{\sigma_{xx}B_{xy} - \sigma_{yx}B_{xx}}{\sigma_{xx}\sigma_{yy} + \sigma_{xy}^{2}} \simeq \frac{B_{xy}}{\sigma_{yy}} - S\frac{\sigma_{xy}}{\sigma_{yy}} + O(H^{2})$$
(8)

The derivation of the above equations is explained in detail in our previous works [17] and indices follow the directions of Fig. 1. Note that in the above only the first term of Ξ which does not depend on H appears in σ_{xx} and B_{xx} and thus in S. On the other hand, due to the parity of velocities, only the second term of Ξ , linear in H, appears in the formulas for σ_{xy} and B_{xy} . Thus the Nernst coefficient is linear in the magnetic field (still in the small field limit where the second term in Ξ is much smaller than the first term).

The workflow of our approach is displayed in Fig. 2. We start with the electronic structure obtained from density functional theory-based codes. The maximally localized Wannier functions [21] (MLWF) are required to represent a fine interpolation of electron energy dispersion followed by the derivation of band velocity and effective mass tensors. Several programs were developed to post-process the scattering rates data provided by various softwares, namely: AMSET [20], ElecTra [22], EPW [23], Perturbo [24], and EPIC STAR [25]. Among those, the interface with ElecTra, AMSET, and Perturbo has been implemented in our code. Specifically, for the case of ElecTra a tutorial was made and added to the GitHub page. Additionally, the user has the option of providing total scattering rates as a function of energy obtained by any package and computing the Nernst coefficient by our code. Relaxation times were then coupled with band-dependent quantities to compute the transport distribution function.

Now that the formalism has been clarified (for more details reference [18] can be consulted), we will proceed to give the details of the first-principles calculations, display and discuss the results in comparison with experimental results.

First-principles calculations 3

In order to calculate the ingredients necessary for the transport distribution function, we have performed first-principles density functional theory (DFT) calculations of three materials, namely Ge, Si, and InSb using the VASP code with PAW pseudopotentials [26, 27]. The PBE [28] exchange-correlation functional yielded zero gaps and nearly linear dispersion around the Gamma point in the conduction bands for Ge and InSb. We, therefore, used the mBJ exchange-correlation functional [29] in order to reproduce the correct band curvature (effective mass) by opening a gap. The mBJ gap is still smaller than that of the experiment and hence the bands were shifted to reproduce the experimental band gaps as the Seebeck coefficient is very sensitive to the latter (more details can be found in the supplementary materials).

Using the WANNIER90 package [21], DFT band structures were then wannierized via maximally localized Wannier functions (MLWF) in order to have a fast calculation of the band energies and velocities on a very fine mesh of k-points in the first Brillouin zone. All the integrals discussed in Section 2 were performed using this data on a fine mesh.

Next, charge carrier relaxation times were calculated by the AMSET code and transformed into energy space. AMSET is an easy to use code that has been successful in reproducing the carrier mobility of many semiconductors and hence we chose to use this code [20]. We note that AMSET does not use a first principles approach. Instead, it uses phenomenological models with inputs either from experiments or first principles. For instance, deformation potential approximation is used for acoustic phonons. An alternative that is computationally more expensive is to use first-principles-based codes such as EPW [23] or Perturbo[24] for electron-phonon scattering rates. Here, we choose to use AMSET as it is enough to reproduce the experimental data. We include acoustic phonon deformation potential, polar optical phonon, piezoelectric, and ionized impurity scattering mechanisms in all three reported materials. A summary of the physical properties used for each material is provided in supplementary materials. These parameters are taken from available experimental data. It is noteworthy to add that alternatively the input parameters for the scattering rates, e.g. deformation potential, dielectric constant, elastic constant, optical phonon frequency, and piezoelectric constant, may be obtained from first-principles DFT methods. Figure 2 summarizes the calculation process of obtaining the band-related parameters and scattering rates separately, and combining them for Nernst calculations.

Lastly, after convergence was reached, we used the output from wannierisation of the bands and scattering rates of AMSET to calculate the transport distribution function Ξ displayed in Eq. 6. Then Ξ was used in equations 2 and 3 to calculate the matrices σ and B. Finally, the isothermal Nernst coefficient was computed from Eq. 1 and compared to available experimental data.

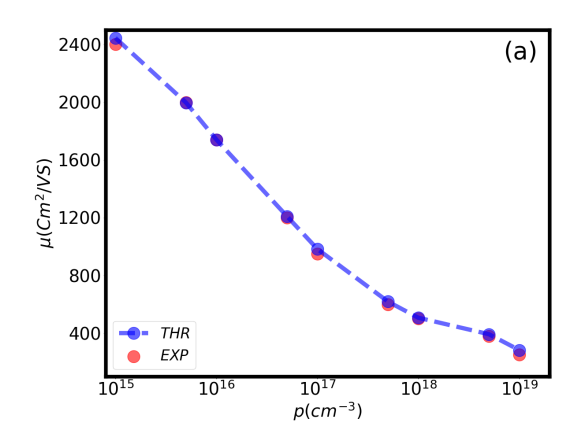
4 Results and discussion

4.1 Germanium

Germanium in its single crystal form is one of the first semiconductors in which the Nernst signal was reported and in fact, it holds the record for the largest Nernst coefficient around room temperature. Therefore, we chose to test our method on Ge. Electrical properties including mobility, electrical resistivity, Seebeck coefficient, and indeed Nernst coefficient largely depend on the scattering rates, thus, the scattering rates and the mobility need to be validated. Fig. 3.a depicts the hole mobility of single crystal Germanium versus doping concentration at room temperature. Fig. 3.b shows the same quantity versus temperature for a hole concentration of $4.9 \times 10^{18} cm^{-3}$. As temperature increases, the population of phonons increases leading to an increase in the electron-phonon scattering rates and a decrease in electron mobility. The acoustic deformation potential scattering and the ionized impurity scatterings are the dominant scattering mechanism in this material and the combination of the two can reproduce the experimental data closely. This fact was also previously reported in the literature [30]. Our theoretical results for Ge are found to be within less than 5% of the experiments. A wide range of values has been reported for the deformation potential, whether in experiments or theory. Therefore, we selected the deformation potentials that best fit the experimental mobility (the value of parameters used are reported in the supplementary material).

The Nernst coefficient of single crystal Ge was measured to be as large as 350 $\mu V/KT$ around room temperature [9]. Yamaguchi [10] also observed extremely large values of the Nernst coefficient for Ge, but they failed to replicate their measurements by a parabolic band model. In this work, we calculate the Nernst coefficient of Ge in a wide range of temperatures using density functional theory.

After the successful replication of Ge mobility (Fig 3), we proceeded with the calculation of the full transport distribution function (Eq. 6) and, finally, evaluated the Nernst coefficient by using Eq. 1. Figure 4 shows that our theory can accurately predict the experimental



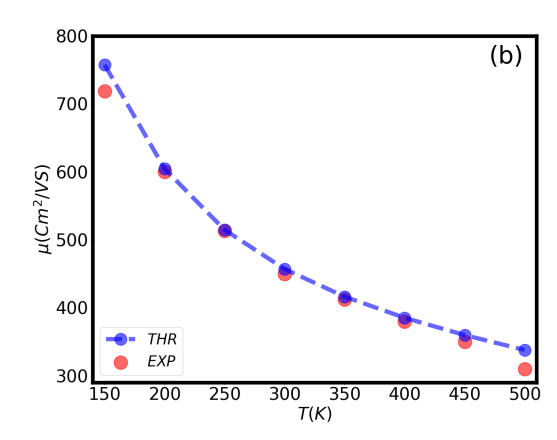


Figure 3: Hole mobility for Germanium at room temperate versus doping concentration (a) and versus temperature (b) for a constant carrier concentration of $4.9 \times 10^{18} Cm^{-3}$. Red circles and blue dashed lines indicate experimental [31] and theoretical data, respectively. The mobilities of Si and InSb are reported in the supplementary material.

Nernst coefficient for Ge in a wide range of temperatures and for various doping concentrations. For a slightly doped sample ($\rho=30\Omega.cm$) the Nernst coefficient continuously decreases versus temperature, though, it decreases less rapidly at high temperatures. The corresponding chemical potential of the electrical resistivity of $\rho=30\Omega.Cm$ is 240 meV below the intrinsic Fermi level. Since we do not know how resistance changes with temperature experimentally, we performed our modeling under constant chemical potential conditions which means chemical potential was kept the same for all temperatures. This assumption breaks at higher temperatures and therefore, we are not able to reproduce the experimental data at temperatures beyond 500K. The dominant carriers are holes. However, the concentration of both electrons and holes increases with the rise in temperature as shown in Fig. 5a. The carrier mobility as shown in Fig. 5b drops as temperature increases. Various models (see Moreau's equation for example) have shown that the Nernst coefficient is proportional to the carrier mobility. In this case, we also observe that the Nernst coefficient follows the carrier mobility trend and decreases with temperature.

Comparing the two samples, the one with larger mobility also exhibits a larger Nernst coefficient. The trend of the Nernst coefficient with respect to temperature is different in the case of the low-resistance sample. Here, as shown in Fig. 4, the Nernst coefficient reaches a maximum value at around 410 K both in theory and experiments. To explain this maximum in the Nernst coefficient, we have plotted the Seebeck coefficient of the two samples in Fig. 5C. In the case of the low-resistance sample, there is a large drop in the Seebeck coefficient vs. temperature at around 400 K which can be in turn attributed to the increase in the population of minority carriers. According to Moreau's relation, the Nernst coefficient is proportional to the slope of the Seebeck coefficient with respect to temperature (represented by the Thomson coefficient). In this case, the maximum of the Nernst coefficient happens when the Thomson coefficient is maximal. We emphasize that Moreau's relation can only qualitatively explain the results and it is not in quantitative agreement with our first-principles model. An alternative explanation is to correlate this maximum to the Seebeck coefficient of the minority carriers. It has been shown that the Nernst coefficient within constant relaxation time approximation and within parabolic bands, comes only from the cross-term between the valence and conduction

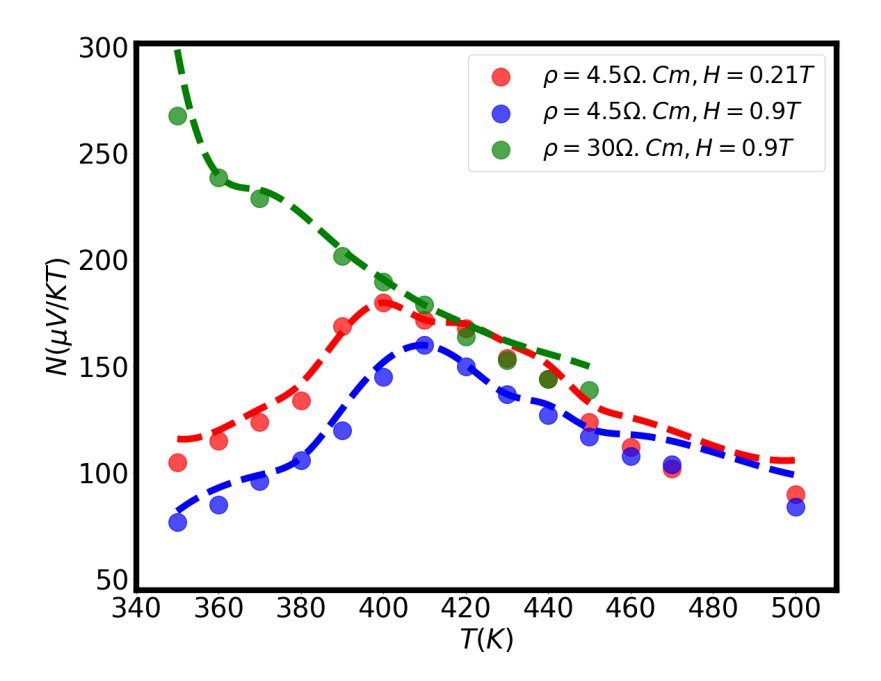


Figure 4: Nernst coefficient of Germanium versus temperature. Solid circles are the experimental data from literature [9] and our theoretical predictions are shown by dashed lines. The two samples have different electrical resistivity (ρ) and are measured under magnetic fields (H) of 0.21 T and 0.9 T.

bands and is proportional to the Seebeck coefficient of the minority carriers (see Eq. 45 of Ref. [32]). At 400 K the minority carriers start to contribute and have a large Seebeck coefficient but of the opposite sign, causing a faster reduction of Seebeck with temperature.

Our findings are normalized to the magnetic field in the units of $(\frac{\mu V}{KT})$ and the Nernst signals appeared to be larger under the smaller magnetic field of 0.21 T compared to 0.9 T whether in experiments or theory (Fig. 4). This is because the denominator is in $1 + aH^2$ causing a further reduction of the Nernst coefficient (see ref [33] and Eq. 8).

4.2 Silicon

Inspired by large Nernst signals of germanium, silicon was thought to show large Nernst signals due to similarities with germanium. Mette studied the Nernst effect in silicon and found that the Nernst coefficient in single-crystal silicon is significantly smaller [34] than that of Ge. This originates from a larger band gap of silicon (1.12 eV versus 0.66 eV in Ge) and smaller carrier mobility (760 cm^2/VS vs 85 cm^2/VS). The band gap in silicon is so wide that the carrier concentration would have a negligible effect far from the band edges. Hence, the Nernst signal will vanish when the chemical potential is deep in the gap. Instead, peak values are expected to appear at the band edges due to maximum relaxation time. It is worth mentioning that in order to achieve the electrical resistivity of 0.22Ω .cm in p-type silicon, it needs to be doped by as much as $8 \times 10^{16} cm^{-3}$, so that the chemical potential moves into the valence band.

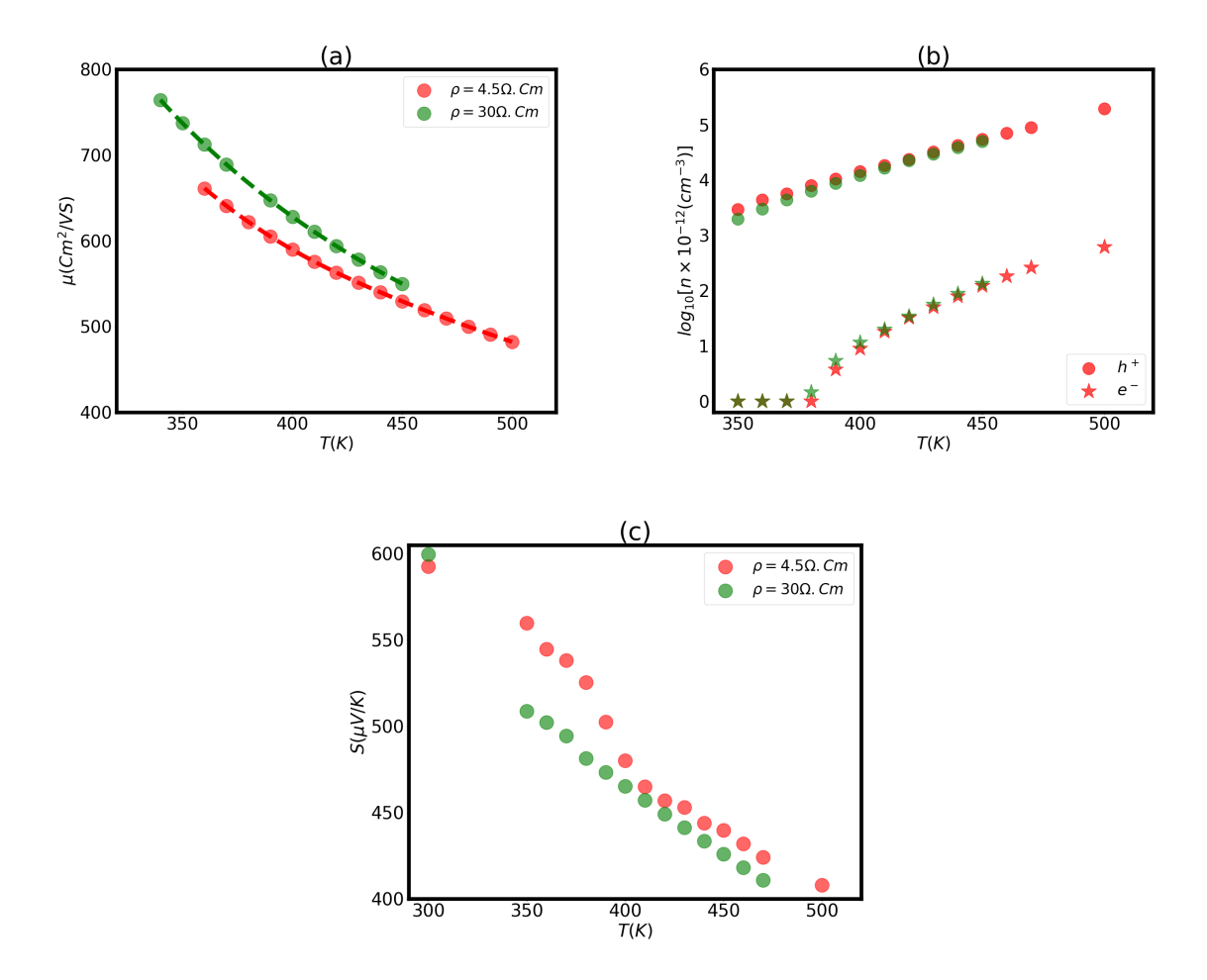


Figure 5: (a) Hole mobility of Germanium samples with the electrical resistivity of 4.5 and 30 $\Omega.cm$ (b) Hole and electron concentrations of Germanium with the electrical resistivity of 4.5 $\Omega.cm$ (red) and 30 $\Omega.cm$ (green) versus temperature. Seebeck coefficient (c) for the same samples versus temperature.

4.3 InSb

Indium antimonide is a narrow gap semiconductor widely used in semiconductor applications e.g. transistors, magnetic field sensors, and infrared cameras [35, 36, 37]. InSb was among the earliest semiconductors that showed relatively large Nernst signals at room temperature. El-saden et.al. reported the Nernst effect in InSb for the first time in the temperature range from 260 to 340 K and applying magnetic fields from 0.4 to 1.2 T. They used a measurement method similar to what Lindberg [38] employed for Hall measurement. The sample length had to be kept at least three times larger than its width to avoid the end electrodes' shorting effect. Decades later, Nakamura [39] carried out thorough measurements of thermoelectric as well as thermomagnetic properties on bridged shape InSb samples and recorded Nernst coefficient values as large as 340 $\mu V/K$. However, his phenomenological model deviates from the experimental results. We performed DFT-based calculations of the Nernst coefficient and found fairly close values to the experiments for a p-type single crystal InSb sample whose electrical conductivity is $2.2 \times 10^4 S/m$ under a magnetic field of 4 T.

Although the hole mobility of InSb is larger than Ge, the chemical potential which yields

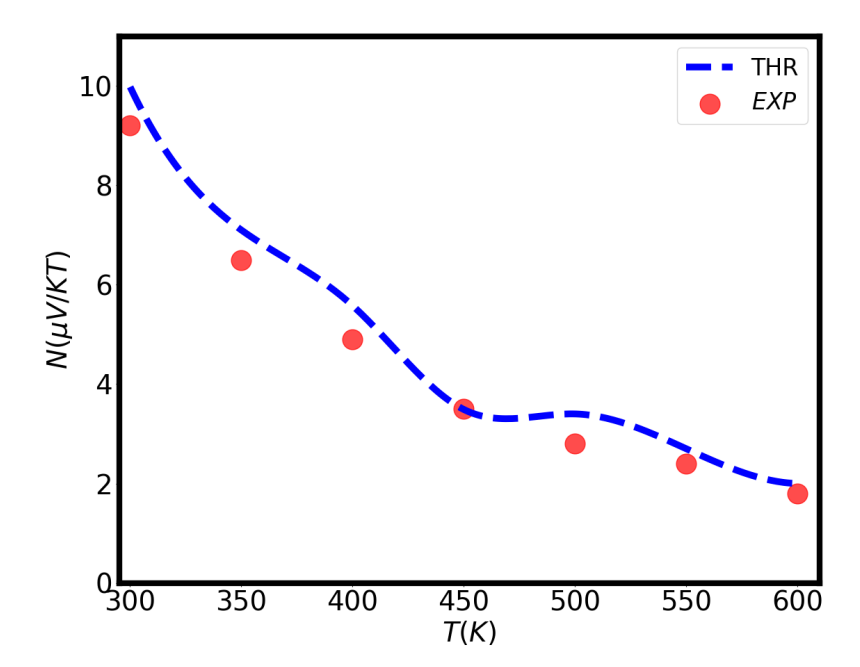


Figure 6: Nernst coefficient of p-type Silicon with $\rho = 0.22\Omega \text{cm}$ at elevated temperatures under a magnetic field of 0.9 Tesla. Our theory (blue dashed line) is in relatively good agreement with the experimental data (red circles) [34].

the electrical conductivity of $2.2\times10^4 S/m$ is in the vicinity of the valence band edge. For a large Nernst signal in semiconductors, minimum coexistence of electrons and holes is desired. The chemical potential that bears the minimum coexistence of the opposite charges occurs at the intrinsic Fermi level. Considering the fact that the product of electron concentration and hole concentration is constant in equilibrium, as the chemical potential moves toward either band, the total concentration of electrons and holes will grow, such that the Nernst signal shrinks due to higher carrier concentration. Moreover, InSb is a narrow gap semiconductor (0.16 eV) so even at room temperature, the intrinsic electron and hole concentrations are substantial, leading to a lower Nernst coefficient in comparison with Ge.

Having the density of states from DFT and the Fermi-Dirac distribution function, we can calculate the electron and hole carrier concentrations at any given temperature and chemical potential. Table 1 summarizes the hole concentration for InSb, Ge, and Si samples studied in this work.

5 Conclusion

In this article, we proposed an efficient approach to compute the Nernst coefficient based on the first-principles density functional theory within the relaxation time approximation. This is a follow-up to our previous work where we reported a first-principles approach based on constant relaxation time approximation [17]. The effect of the band structure on the Nernst coefficient can be obtained within constant relaxation time approximation. However, to enable comparison with the experiment, it is crucial to include the electron's energy-dependent relaxation times. In this work, we account for the charge carrier relaxation time caused by various mechanisms

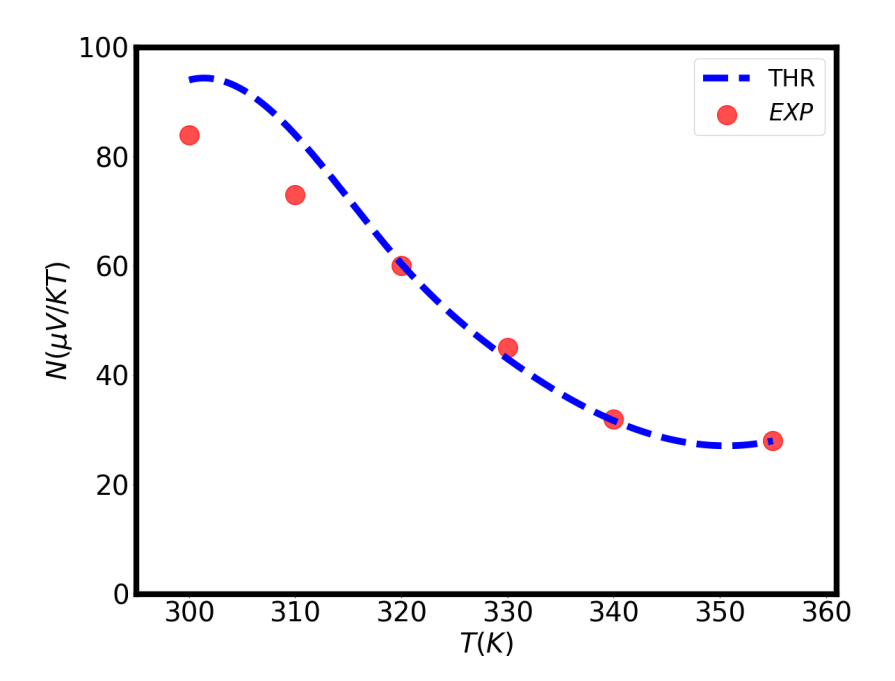


Figure 7: Nernst coefficient of p-doped Indium antimonide as a function of temperature at 4 Tesla. Red circles are the measurements from Ref [11] and values obtained by our approach are shown by the blue dashed line.

including phonons and ionized impurity scatterings. In contrast to phenomenological models, in our approach band structures are based on MLWFs coming from first-principles calculations, while relaxation times can either be calculated from first principles, or obtained from simplified models with one or two fitting parameters. In order to validate the method, our findings were compared to experimental data on Ge, InSb, and Si. The effects of experimental conditions such as temperature, doping concentration, and strength of the magnetic field were investigated and a remarkable accuracy was observed with a moderate computational cost. This approach is applicable within the validity of the inputs, that is within the validity of the DFT framework and the validity of the codes or models used to compute relaxation rates. It paves the way for the materials discovery and prediction of promising candidates for applications based on the Nernst effect.

Acknowledgements

The authors acknowledge support from NSF grant # 2230352 for the support of this work. The Rivanna cluster of UVA was used for these computations.

Credit author statement

Emad Rezaei: Programming the Code, Performing and Analyzing the Data, Paper writing. Mona Zebarjadi: Defining the project, Supervision of the work, Analyzing the data, reviewing and editing the paper. Keivan Esfarjani: Coding, Supervision of the work, Analyzing the data, reviewing and editing the paper.

Declaration of competing interest

The authors declare that there are no personal relationships or competing financial interests

Table 1: Hole concentration at 300 K for p-type InSb, Ge, and Si samples studied in this work.

Material	Hole concentration (cm^{-3})	$\rho(\Omega.cm)$
InSb	1.16×10^{17}	4.5×10^{-5}
Ge Ge	$1.2 \times 10^{15} \\ 2.8 \times 10^{15}$	30.00 4.5
Si	8×10^{16}	0.22

that could affect this work.

Data availability

The raw data and source code required to reproduce these results are available to download from S.E.R's GitHub page.

References

- [1] I. Maghami, V. A. Sobral, M. M. Morsy, J. C. Lach, J. L. Goodall, Exploring the complementary relationship between solar and hydro energy harvesting for self-powered water monitoring in low-light conditions, Environmental Modelling & Software 140 (2021) 105032.
- [2] W. Wang, V. Cionca, N. Wang, M. Hayes, B. O'Flynn, C. O'Mathuna, Thermoelectric energy harvesting for building energy management wireless sensor networks, International journal of distributed sensor networks 9 (6) (2013) 232438.
- [3] Z. Yuan, X. Tang, Z. Xu, J. Li, W. Chen, K. Liu, Y. Liu, Z. Zhang, Screen-printed radial structure micro radioisotope thermoelectric generator, Applied Energy 225 (2018) 746–754.
- [4] S. Bogason, Cryogenic cooling with a single crystal bismuth nernst-ettingshausen cooler, Ph.D. thesis, The Ohio State University (2018).
- [5] H. Goldsmid, K. Sydney, A thermal radiation detector employing the nernst effect in cd3as2-nias, Journal of Physics D: Applied Physics 4 (6) (1971) 869.
- [6] M. Mizuguchi, S. Nakatsuji, Energy-harvesting materials based on the anomalous nernst effect, Science and technology of advanced materials 20 (1) (2019) 262–275.
- [7] A. Ettingshausen, W. Nernst, Ueber das auftreten electromotorischer kräfte in metallplatten, welche von einem wärmestrome durchflossen werden und sich im magnetischen felde befinden, Ann. Phys. Chem. 265 (1886) 343.
- [8] K. Behnia, The nernst effect and the boundaries of the fermi liquid picture, Journal of Physics: Condensed Matter 21 (11) (2009) 113101.
- [9] H. Mette, W. W. Gärtner, C. Loscoe, Nernst and ettingshausen effects in germanium between 300 and 750 k, Physical Review 115 (3) (1959) 537.

- [10] K. Ikeda, H. Nakamura, I. Yanenaga, S. Yamaguchi, Transport coefficients of ge in magnetic fields, in: Seventeenth International Conference on Thermoelectrics. Proceedings ICT98 (Cat. No. 98TH8365), IEEE, 1998, pp. 277–279.
- [11] H. N. H. Nakamura, K. I. K. Ikeda, S. Y. S. Yamaguchi, Transport coefficients of indium antimonide in a magnetic field, Japanese journal of applied physics 38 (10R) (1999) 5745.
- [12] R. Delves, Thermomagnetic effects in semiconductors and semimetals, Reports on Progress in Physics 28 (1) (1965) 249.
- [13] M. Cutler, N. F. Mott, Observation of anderson localization in an electron gas, Physical Review 181 (3) (1969) 1336.
- [14] A. Avery, M. Pufall, B. L. Zink, Determining the planar nernst effect from magnetic-field-dependent thermopower and resistance in nickel and permalloy thin films, Physical Review B 86 (18) (2012) 184408.
- [15] M. Matusiak, M. Babij, T. Wolf, Anisotropy of the seebeck and nernst coefficients in parent compounds of the iron-based superconductors, Physical Review B 97 (10) (2018) 100506.
- [16] S. J. Watzman, T. M. McCormick, C. Shekhar, S.-C. Wu, Y. Sun, A. Prakash, C. Felser, N. Trivedi, J. P. Heremans, Dirac dispersion generates unusually large nernst effect in weyl semimetals, Physical Review B 97 (16) (2018) 161404.
- [17] S. E. Rezaei, M. Zebarjadi, K. Esfarjani, Calculation of thermomagnetic properties using first-principles density functional theory, Computational Materials Science 210 (2022) 111412.
- [18] M. Zebarjadi, E. Rezaei, S. Akhanda, K. Esfarjani, Nernst coefficient within relaxation time approximation, Physical Review B 103 (14) (2021) 144404.
- [19] G. Pizzi, D. Volja, B. Kozinsky, M. Fornari, N. Marzari, Boltzwann: A code for the evaluation of thermoelectric and electronic transport properties with a maximally-localized wannier functions basis, Computer Physics Communications 185 (1) (2014) 422–429.
- [20] A. M. Ganose, J. Park, A. Faghaninia, R. Woods-Robinson, K. A. Persson, A. Jain, Efficient calculation of carrier scattering rates from first principles, Nature communications 12 (1) (2021) 1–9.
- [21] A. A. Mostofi, J. R. Yates, Y.-S. Lee, I. Souza, D. Vanderbilt, N. Marzari, wannier90: A tool for obtaining maximally-localised wannier functions, Computer physics communications 178 (9) (2008) 685–699.
- [22] P. Graziosi, Z. Li, N. Neophytou, Electra code: Full-band electronic transport properties of materials, Computer Physics Communications 287 (2023) 108670.
- [23] J. Noffsinger, F. Giustino, B. D. Malone, C.-H. Park, S. G. Louie, M. L. Cohen, Epw: A program for calculating the electron–phonon coupling using maximally localized wannier functions, Computer Physics Communications 181 (12) (2010) 2140–2148.
- [24] J.-J. Zhou, J. Park, I.-T. Lu, I. Maliyov, X. Tong, M. Bernardi, Perturbo: A software package for ab initio electron-phonon interactions, charge transport and ultrafast dynamics, Computer Physics Communications 264 (2021) 107970.

- [25] T. Deng, G. Wu, M. B. Sullivan, Z. M. Wong, K. Hippalgaonkar, J.-S. Wang, S.-W. Yang, Epic star: a reliable and efficient approach for phonon-and impurity-limited charge transport calculations, npj Computational Materials 6 (1) (2020) 46.
- [26] J. Hafner, Ab-initio simulations of materials using vasp: Density-functional theory and beyond, Journal of computational chemistry 29 (13) (2008) 2044–2078.
- [27] G. Kresse, D. Joubert, From ultrasoft pseudopotentials to the projector augmented-wave method, Physical review b 59 (3) (1999) 1758.
- [28] J. P. Perdew, K. Burke, Y. Wang, Generalized gradient approximation for the exchange-correlation hole of a many-electron system, Physical review B 54 (23) (1996) 16533.
- [29] F. Tran, P. Blaha, Accurate band gaps of semiconductors and insulators with a semilocal exchange-correlation potential, Physical review letters 102 (22) (2009) 226401.
- [30] V. Aubry-Fortuna, P. Dollfus, Electron transport properties in high-purity ge down to cryogenic temperatures, Journal of Applied Physics 108 (12) (2010) 123706.
- [31] O. Golikova, B. Y. Moizhes, L. Stilbans, Hole mobility of germanium as a function of concentration and temperature, Soviet Physics-Solid State 3 (10) (1962) 2259–2265.
- [32] M. Zebarjadi, S. E. Rezaei, M. S. Akhanda, K. Esfarjani, Nernst coefficient within relaxation time approximation, Physical Review B 103 (14) (2021) 144404.
- [33] C. Jacoboni (Ed.), Theory of electron transport in semiconductors: a pathway from elementary physics to nonequilibrium Green functions, Springer Science & Business Media, New York, 2010.
- [34] H. Mette, W. W. Gärtner, C. Loscoe, Nernst and ettingshausen effects in silicon between 300° k and 800° k, Physical Review 117 (6) (1960) 1491.
- [35] T. Ashley, A. Dean, C. T. Elliott, R. Jefferies, F. Khaleque, T. Phillips, High-speed, low-power insb transistors, in: International Electron Devices Meeting. IEDM Technical Digest, IEEE, 1997, pp. 751–754.
- [36] J. L. Pipher, W. J. Forrest, W. J. Glaccum, R. G. Benson, D. J. Krebs, M. D. Jhabvala, J. P. Rosbeck, N. A. Lum, W. Lum, J. D. Garnett, et al., Insb arrays for irac (infrared array camera) on sirtf (space infrared telescope facility), in: Infrared Spaceborne Remote Sensing VIII, Vol. 4131, SPIE, 2000, pp. 7–12.
- [37] I. Shibasaki, Properties of insb thin films grown by molecular beam epitaxy and their applications to magnetic field sensors, IEEJ Transactions on Sensors and Micromachines 123 (3) (2003) 69–78.
- [38] O. Lindberg, Hall effect, Proceedings of the IRE 40 (11) (1952) 1414–1419.
- [39] H. Nakamura, K. Ikeda, S. Yamaguchi, Physical model of nernst element, in: Seventeenth International Conference on Thermoelectrics. Proceedings ICT98 (Cat. No. 98TH8365), IEEE, 1998, pp. 97–100.